Early Ultra-Violet observations of type IIn supernovae constrain the asphericity of their circumstellar material

Maayane T. Soumagnac,[1,2] Eran O. Ofek,[2] Jingyi Liang,[2] Avishay Gal-yam,[2] Peter Nugent,[1,3] Yi Yang,[2] S. Bradley Cenko,[4] Jesper Sollerman,[5] Daniel A. Perley,[6] Igor Andreoni,[7] Cristina Barbarino,[5] Kevin B. Burdge,[7] Rachel J. Bruch,[2] Kishalay De,[7] Alison Dugas,[7] Christoffer Fremling,[7] Melissa L. Graham,[8] Matthew J. Hankins,[7] Shane Moran,[9,10] James D. Neill,[7] Steve Schulze,[2] Brigitta M. Sipőcz,[11] Leonardo Tartaglia,[5] Richard Walters,[7] Lin Yan,[7] Yuhan Yao,[7] and Ofer Yaron[2]

[1] *Lawrence Berkeley National Laboratory, 1 Cyclotron Road, Berkeley, CA 94720, USA*
[2] *Department of Particle Physics and Astrophysics, Weizmann Institute of Science, Rehovot 76100, Israel*
[3] *Department of Astronomy, University of California, Berkeley, CA 94720-3411, USA*
[4] *Astrophysics Science Division, NASA Goddard Space Flight Center, MC 661, Greenbelt, MD 20771, USA*
[5] *The Oskar Klein Centre, Department of Astronomy, Stockholm University, AlbaNova, 10691 Stockholm, Sweden*
[6] *Astrophysics Research Institute, Liverpool John Moores University, 146 Brownlow Hill, Liverpool L3 5RF, UK*
[7] *California Institute of Technology, 1200 East California Boulevard, MC 278-17, Pasadena, CA 91125, USA*
[8] *Department of Astronomy, University of Washington, Box 351580, U.W., Seattle, WA 98195-1580, USA*
[9] *Tuorla Observatory, Department of Physics and Astronomy, FI-20014, University of Turku, Finland*
[10] *Nordic Optical Telescope, Apartado 474, E-38700 Santa Cruz de La Palma, Spain*
[11] *DIRAC Institute, Department of Astronomy, University of Washington, Seattle, WA 98195, USA*

Submitted to ApJ

ABSTRACT

We present a survey of the early evolution of Type IIn supernovae (SNe IIn) in the Ultra-Violet (UV) and visible light and show that at least one third of them appear to explode in aspherical circumstelllar clouds. Our sample consists of 12 SNe IIn discovered and observed with the Zwicky Transient Facility (ZTF) and followed-up in the UV with the Neil Gehrels Swift Observatory. We use these observations to constrain the geometry of the circumstellar material (CSM) surrounding SN IIn explosions, which may shed light on their progenitor diversity. Indeed, while observations of SNe IIn are usually analyzed within the framework of spherically symmetric models of CSM, resolved images of stars undergoing considerable mass loss suggest that asphericity is common, and should be taken into account for realistic modeling of these events. We apply the criterion for asphericity introduced by Soumagnac et al. (2019b), stating that a fast increase of the blackbody effective radius, if observed at times when the CSM surrounding the explosion is still optically thick, may be interpreted as an indication that the CSM is aspherical. We find that two thirds of the SNe in our sample show evidence for aspherical CSM, whereas one third do not show evidence for either spherical or aspherical CSM. After correcting for the relative volume of these two sub-classes, we derive a conservative lower limit of 35% on the fraction of SNe IIn showing evidence for aspherical CSM.

Keywords: keywords

1. INTRODUCTION

Type IIn supernovae (SNe IIn) show prominent and narrow-to-intermediate width Balmer emission lines in their spectra (Schlegel 1990; Filippenko 1997; Smith 2014; Gal-Yam 2017). This specificity is thought to be the signature of photoionized and dense, hydrogen-rich, circumstellar medium (CSM) which is ejected from the SN progenitor prior to its explosive death. Because these narrow lines are the signature of an external physical phenomenon rather than of any intrinsic property of the explosion, they may appear in the spectra of many SNe,

Corresponding author: Maayane T. Soumagnac
mtsoumagnac@lbl.gov

at some point during their evolution. As a result, the Type IIn class of SNe is a heterogeneous category of objects. Depending on the spatial distribution and physical properties of the CSM surrounding the explosion, the characteristic narrow Balmer lines may persist for days ("flash spectroscopy", Gal-Yam et al. 2014; Khazov et al. 2016; Yaron et al. 2017), weeks (e.g., SN 1998S, Li et al. 1998; Fassia et al. 2000, 2001; SN 2005gl, Gal-Yam et al. 2007; SN 2010mc, Ofek et al. 2013a), or years (e.g., SN 1988Z, Danziger & Kjaer 1991; Stathakis & Sadler 1991; Turatto et al. 1993; van Dyk et al. 1993; Chugai & Danziger 1994; Fabian & Terlevich 1996; Aretxaga et al. 1999; Williams et al. 2002; Schlegel & Petre 2006; Smith et al. 2017; SN 010 jl, Patat et al. 2011; Stoll et al. 2011; Gall et al. 2014; Ofek et al. 2014).

Observing SNe IIn at ultraviolet (UV) wavelengths is interesting for several reasons. First, an important ingredient of the physical picture governing SNe IIn explosions - the collisionless shock propagating in the CSM after the shock breakout (Ofek et al. 2010) - is predicted to radiate most in the UV and X-rays (Katz et al. 2011; Murase et al. 2011, 2014; Chevalier & Irwin 2012). Observing the explosion at these wavelengths has the potential to unveil precious information about the explosion mechanism and the CSM properties (e.g., Ofek et al. 2013b). In particular, it may provide a much better estimate of the bolometric luminosity of the event.

Second, UV observations can help constrain the geometrical distribution of the CSM, which is closely related to the mass-loss processes occurring before the explosion and probe the nature of the progenitors of this type of events.

Although observations of SNe IIn are usually analyzed within the framework of spherically symmetric models of CSM, resolved images of stars undergoing considerable mass loss (e.g., η Carinae; Davidson & Humphreys 1997, 2012), some of whom are likely SN IIn progenitors (Gal-Yam et al. 2007; Gal-Yam & Leonard 2009) as well as polarimetric observations (Leonard et al. 2000; Hoffman et al. 2008; Wang & Wheeler 2008; Reilly et al. 2017) suggest that asphericity should be taken into account for more realistic modeling. Asphericity of the CSM has recently been invoked to interpret the spectrocopic and spectropolarimetric observations of the Type IIn SN 2012ab (Bilinski et al. 2017) and SN 2009ip (Mauerhan et al. 2014; Smith et al. 2014; Levesque et al. 2014; Reilly et al. 2017).

In Soumagnac et al. (2019b), we showed that the light curve of the luminous Type IIn SN PTF 12glz may be interpreted as evidence for aspherical CSM. While the spectroscopic analysis is consistent with opaque CSM obstructing our view of any growing structure, r_{BB} - the radius of the deepest transparent emitting layer - grows by an order of magnitude, at a speed of $\sim 8000\,\mathrm{km\,s^{-1}}$. To explain this tension, we considered a simple aspherical structure of CSM: a slab. We modeled the radiation from an explosion embedded in a slab of CSM by numerically solving the radiative diffusion equation in a slab with different density profiles: $\rho = Const.$, $\rho \propto |z|^{-1}$ and a wind density profile $\rho \propto z^{-2}$. Although this model is simplistic, it allows recovery of the peculiar growth of the blackbody radius r_{BB} observed in the case of PTF 12glz, as well as the decrease of its blackbody temperature T_{BB}.

This allowed us to derive a criterion for asphericity: a fast increase of r_{BB} can be interpreted as the signature of non-spherical CSM, if it is observed while the CSM is still optically thick. This is because the approximately stationary CSM is obscuring the expanding SN ejecta, and explaining an expanding emitting region due to photon diffusion in the CSM requires a non-spherical CSM configuration. In this paper, we assemble a sample of SNe IIn, to which we apply this criterion in order to estimate the fraction of SNe IIn showing evidence for non-spherical CSM.

Several samples of SNe IIn have been gathered and studied so far. Among them, the sample by Kiewe et al. (2012), consists of four SNe IIn observed by the Caltech Core-Collapse Project (CCCP) with the 1.5 m robotic telescope at the Palomar Observatory (P60; Cenko et al. 2006) using JohnsonCousins BVRI filters. They studies the light curve features and derived the progenitor star wind velocities. The sample by Taddia et al. (2013) consists of 5 SNe IIn observed by the Carnegie Supernova Project (Hamuy et al. 2006) at visible-light and near-infrared wavelengths, and was used to derive mass-loss parameters. The sample by Ofek et al. (2014) consists of 19 SNe IIn observed by the Palomar Transient Factory (Law et al. 2009; Rau et al. 2009) and its extension, the intermediate PTF (iPTF) using the PTF R-band filter. It allowed to exhibit a possible correlation between the r-band rise time and peak luminosity of SNe IIn and to derive a lower limits on the shock-breakout velocity, supporting the idea that early-time light curves of SNe IIn are caused by shock breakout in a dense CSM. The sample by Nyholm et al. (2019) consists of 42 objects with observations from PTF and iPTF, and was was used for an in-depth study of their light-curve properties. de la Rosa et al. (2016) collected Swift UV observations of 10 SNe IIn observed between 2007 and 2013 (8 of which post-peak) and studied e.g. their blackbody properties. To our knowledge, no systematic and planned survey of the early phase of SNe IIn in the UV has been performed so far. In this paper, we present a sample of 12 SNe IIn detected and observed by the Zwicky Transient Facility (ZTF) (e.g., Bellm et al. 2019; Graham et al. 2019) and followed-up in the UV by the Neil Gehrels Swift Observatory (*Swift*) space telescope (Gehrels et al. 2004).

We present the aforementioned observations in §2. In §3, we present some analysis of these observations. §4 is dedicated to constraining the fraction of SNe IIn exploding into aspherical CSM. We summarize our main results in §5.

2. OBSERVATIONS AND DATA REDUCTION

In this section, we present the ZTF and *Swift* observations of the 12 SNe IIn of our sample.

2.1. *Discovery*

All 12 SNe IIn were detected by the ZTF automatic pipeline as potential transients in the data from the ZTF camera mounted on the 1.2 m Samuel Oschin telescope (P48, Rahmer et al. 2008). The host galaxies r-band magnitudes, as well as the coordinates, redshift and distance modulus of all objects are summarized in Table 1. The Milky Way extinction was deduced from Schlafly & Finkbeiner (2011) using the extinction curves of Cardelli et al. (1989).

2.2. *Selection criterion*

Since the beginning of operation, ZTF has found several spectroscopically confirmed SNe IIn per month. However, applying the criterion for asphericity from Soumagnac et al. (2019b) depends on our ability to measure the evolution of $r_{\rm BB}$ - the effective blackbody radius - at the time when the CSM is still optically thick and obstructing our view of any expanding material. We selected only SNe IIn which were spectroscopically confirmed while still on their rise. This selection criterion was motivated by two reasons (1) the spectrum of the SNe IIn in ths early phase is still well described by a blackbody spectrum (2) the rise of the optical light curve gives a better handle on the evolution of $r_{\rm BB}$ than the peak phase (3) we assumed that rising SNe IIn are young enough to allow us to take several *Swift* observations and still be in the regime where expanding material has not reached optically thin areas of the CSM. Some of these objects were first reported and classified by other surveys, see Table 1 for details.

2.3. *Photometry*

All the light curves are shown in Figure 1. The photometry is reported in electronic Table 2 and is available via WISeREP[1].

Photometry was obtained using the ZTF camera mounted on the P48 telescope, through the P48 r and g filters. Data were obtained with a cadence of about $1-3$ days, to a limiting AB magnitude of r ≈ 20.5 mag and g ≈ 21 mag. The P48 data were automatically reduced using the ZTF pipeline (Masci et al. 2019), using the image subtraction algorithm `ZOGY` by Zackay et al. (2016).

The robotic 1.52 m telescope at Palomar (P60; Cenko et al. 2006) was used with a 2048 × 2048-pixel "Rainbow" CCD camera (Ben-Ami et al. 2012; Blagorodnova et al. 2018) and g', r', i' SDSS filters. Data reduction of the P60 data was performed using the FPipe pipeline (Fremling et al. 2016), using the image subtraction algorithm by Zackay et al. (2016).

The *Swift* UVOT data were retrieved from the NASA Swift Data Archive[2] and reduced using standard software distributed with HEAsoft version 6.26[3]. Photometry was measured using the FTOOLSs `uvotimsum` and `uvotsource` with a 5 circular aperture.

None of the SNe IIn in our sample were detected with the *Swift* XRT camera.

2.4. *Spectroscopy*

Optical spectra of all SNe were obtained using the telescopes and spectrographs listed in Table 3. The spectra were used to determine the redshift from the narrow host lines (Hα). All the spectra were corrected for Galactic extinction as deduced from Schlafly & Finkbeiner (2011), using Cardelli et al. (1989) extinction curves.

All spectra are shown in Figure 2 and are available from WISeREP. In the following, we summarize the reduction procedures applied for each spectrum. All spectroscopic observations were calibrated in the following way: since we have contemporaneous P48 r-band data, all spectra were scaled so that their synthetic photometry matches the P48 r-band value.

The Spectral Energy Distribution Machine (SEDm, Ben-Ami et al. 2012; Blagorodnova et al. 2018) spectra were automatically reduced by the IFU data reduction pipeline (Rigault et al. 2019).

The SPRAT spectra were processed by a modification of the pipeline for FrodoSpec (Barnsley et al. 2012).

The spectra taken with the Andalucia Faint Object Spectrograph and Camera (ALFOSC), mounted on the

[1] https://wiserep.weizmann.ac.il

[2] https://heasarc.gsfc.nasa.gov/cgi-bin/W3Browse/swift.pl

[3] https://heasarc.nasa.gov/lheasoft/

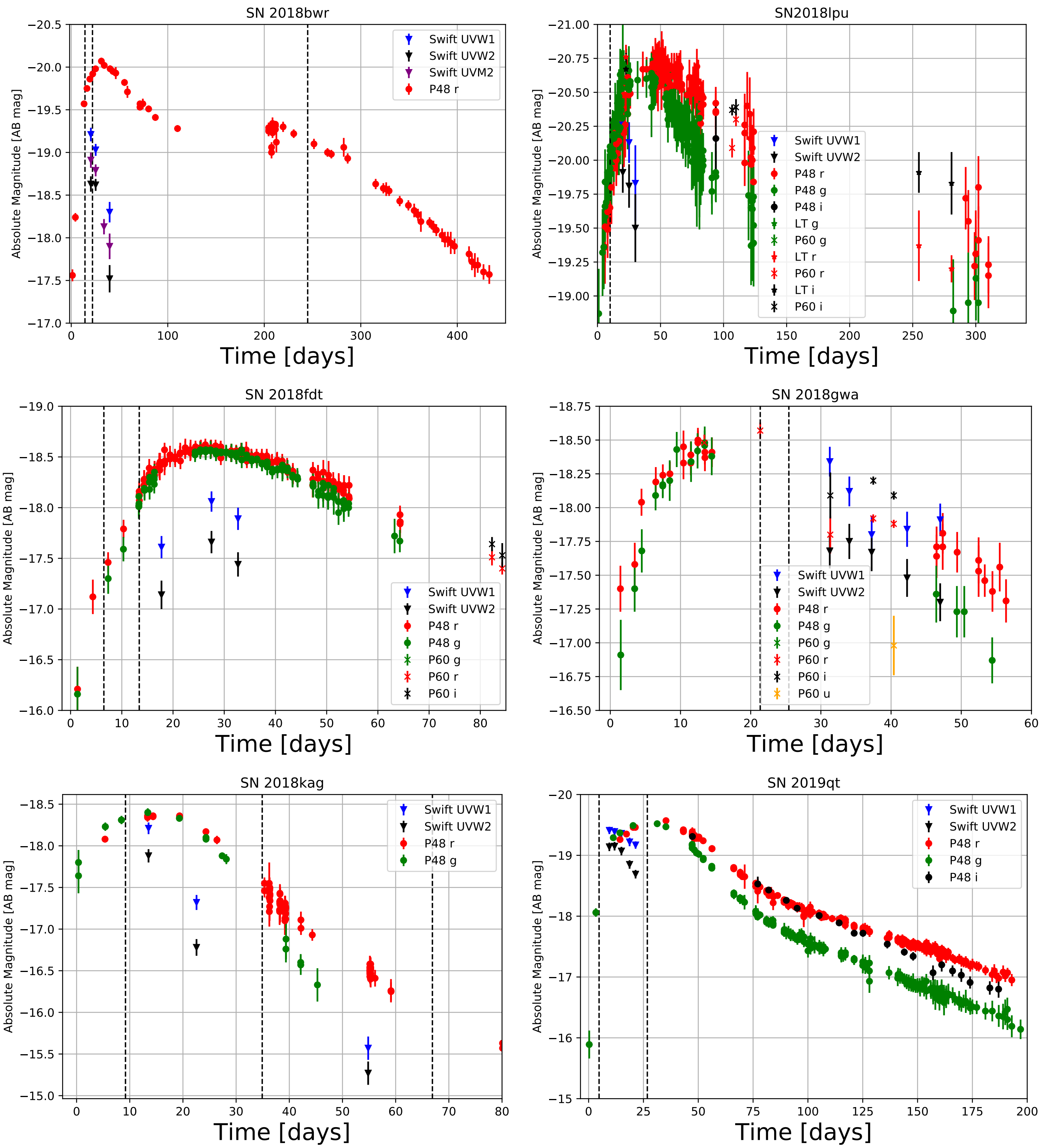
SN 2018bwr
Swift UVW1
Swift UVW2
Swift UVM2
P48 r
Absolute Magnitude [AB mag]
Time [days]
SN2018lpu
Swift UVW1
Swift UVW2
P48 r
P48 g
P48 i
LT g
P60 g
LT r
P60 r
LT i
P60 i
Absolute Magnitude [AB mag]
Time [days]
SN 2018fdt
Swift UVW1
Swift UVW2
P48 r
P48 g
P60 g
P60 r
P60 i
Absolute Magnitude [AB mag]
Time [days]
SN 2018gwa
Swift UVW1
Swift UVW2
P48 r
P48 g
P60 g
P60 r
P60 i
P60 u
Absolute Magnitude [AB mag]
Time [days]
SN 2018kag
Swift UVW1
Swift UVW2
P48 r
P48 g
Absolute Magnitude [AB mag]
Time [days]
SN 2019qt
Swift UVW1
Swift UVW2
P48 r
P48 g
P48 i
Absolute Magnitude [AB mag]
Time [days]

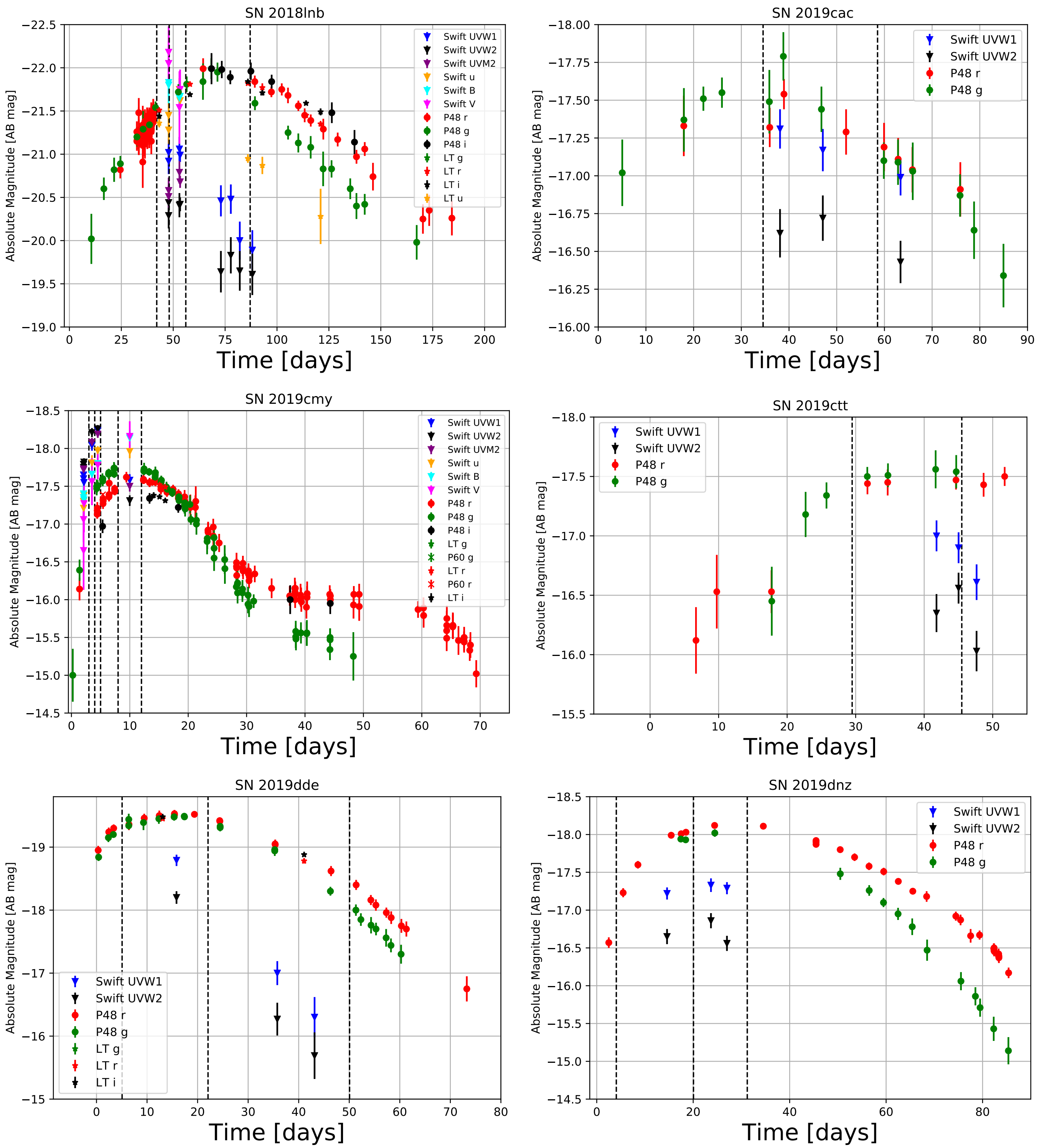

Figure 1. The light curves of all the objects in our sample. Time is shown relative to the estimated epoch at which the extrapolated light curve (Equation A1 and Equation A2) is reaching zero: t_0, as derived in § 3.1 and summarized in Table 4. The x-axis starts at the most recent non-detection, used as the lower limit of the prior in the t_0 fit. Black dashed lines indicate dates at which spectroscopic data exist.

Table 1. Summary of observational parameters

IAU Name	ZTF Name	RA (deg)	Dec (deg)	Redshift	Distance modulus (mag)	Galactic extinction E_{B-V} (mag)
SN 2018lpu	ZTF18abgrlpv	283.937395	+47.441250	0.2104	40.10	0.055
SN 2018fdt	ZTF18abltfho	256.184755	+38.235567	0.055	36.91	0.036
SN 2018gwa	ZTF18abxbhov	110.069724	+41.346650	0.0659	37.33	0.075
SN 2018bwr	ZTF18aavskep	232.109019	+8.806157	0.046	36.50	0.036
SN 2018kag	ZTF18acwzyor	133.951981	+3.5841530	0.02736	35.33	0.045
SN 2019qt	ZTF19aadgimr	224.794385	+43.819899	0.035	35.88	0.017
SN 2018lnb	ZTF19aaadwfi	159.5836458	+48.2752905	0.222	40.23	0.012
SN 2019cac	ZTF19aaksxgp	207.5882959	-2.5069478	0.0467	36.53	0.049
SN 2019cmy	ZTF19aanpcep	227.2118487	+40.7137497	0.0314	35.58	0.015
SN 2019ctt	ZTF19aanfqug	150.176198	+12.039836	0.0464	36.50	0.037
SN 2019dde	ZTF19aaozsuh	217.05016	-1.5804196	0.06	37.11	0.052
SN 2019dnz	ZTF19aaqasrq	297.131153	+2.91375	0.025	35.13	0.183

NOTE—The three first SNe are those for which we were unable to secure enough spectroscopic data in order to include them in our analysis of the CSM geometry (see § 3.3). SN 2018lpu was discovered and classified by the ZTF survey; SN 2018fdt was discovered by the ATLAS survey on 2018-08-14 as ATLAS18tuy (Tonry et al. 2018b), also detected by Gaia surveys as Gaia18chl, classified by ZTF (Fremling et al. 2018a); SN 2018gwa was discovered (Fremling 2018) and classified (Fremling et al. 2018b) by ZTF, also detected by Gaia on 2018-10-05 as Gaia18cxl; The rest of the SNe in the table are all inclded in our analysis of the CSM geometry. SN 2018bwr was discovered by the ATLAS survey on 2018-05-21 as ATLAS18ppb (Tonry et al. 2018a), also detected by PS1 and Gaia surveys as PS18aau and Gaia18bpl, classified by ZTF (Fremling & Sharma 2018); SN 2018kag was discovered by the ASAS-SN survey on 2018-12-17 as ASASSN-18abt and classified by Prentice et al. (2018); SN 2019qt was discovered (Nordin et al. 2019a) and classified (Payne et al. 2019) by ZTF, also detected by ATLAS, Gaia and PS1 as ATLAS19btl, Gaia19aid and PS19ahv; SN 2018lnb was discovered and classified by ZTF (Fremling et al. 2019a); SN 2019cac was discovered and classified by ZTF (Fremling 2019a), also detected by ATLAS and PS1 as ATLAS19doj and PS19ym; SN 2019cmy was discovered (Nordin et al. 2019b) and classified (Fremling et al. 2019b) by ZTF, also detected by ATLAS as ATLAS19elx; SN 2019ctt was discovered by ZTF (Nordin et al. 2019c) and classified by SCAT (Tucker et al. 2019); SN 2019dnz was discovered by ZTF (Fremling 2019b) and classified by TCD (Prentice et al. 2019), also detected by ATLAS as ATLAS19hra; SN 2019dde was discovered by ZTF, classified by ZTF (Fremling et al. 2019c) and (Cartier et al. 2019), also detected by MASTER and PS1 as MASTER OT J142812.05-013615.2 and PS19aaa.

2.56-meter Nordic Optical Telescope (NOT), were reduced following standard IRAF[4] procedures.

The spectra taken with the Auxiliary-port CAMera (ACAM), mounted on the 4.2-m William Herschel Telescope (WHT), were processed following standard IRAF procedures.

The data from the Double Beam Spectrograph (DBSP) on the Palomar 200-inch (P200) telescope were reduced following standard IRAF procedures of long slit spectroscopy. The two-dimensional (2D) images were first bias subtracted and flatfield-corrected, then the 1D spectral spectra were extracted, wavelength calibrated with comparison lamps, and flux calibrated using observations of spectrophotometric standard stars observed during the same night and at approximately similar airmasses to the SN.

The spectra taken with the SuperNova Integral Field Spectrograph (SNIFS; Aldering et al. 2002; Lantz et al. 2004) were obtain from TNS with kind permission from Anna V Payne and Michael A. Tucker.

Data taken with the FLOYDS spectrograph mounted on the 2m Faulkes Telescope North, Hawaii, USA through the observing program TAU2019A-008 (PI: Ofek). A 1.″2 slit was placed on the target. The spectrum was extracted and calibrated following standard

[4] IRAF is distributed by the National Optical Astronomy Observatories, which are operated by the Association of Universities for Research in Astronomy, Inc., under cooperative agreement with the National Science Foundation.

Table 2. Photometry

Object	Epoch	Mag	Magerr	Flux	Fluxerr	Abs. mag	Abs. magerr	Filter	Instrument
(JD)	(AB)	(AB)	(erg/s)	(erg/s)	(AB)	(AB)			
ZTF18aavskep	2458273.8166	16.75	0.01	$5.267e-16$	$0.049e-16$	−19.75	0.01	r	ZTF+P48
ZTF19aadgimr	2458502.9868	16.59	0.04	$1.097e-15$	$0.040e-15$	−19.29	0.04	g	ZTF+P48
ZTF19aadgimr	2458586.8067	17.75	0.04	$1.366e-16$	$0.050e-16$	−18.13	0.04	i	ZTF+P48
ZTF18aavskep	2458277.8361	17.87	0.09	$1.833e-15$	$0.152e-15$	−18.63	0.09	$UVW2$	Swift+UVOT
ZTF18aavskep	2458277.8383	17.58	0.09	$2.004e-15$	$0.166e-15$	−18.91	0.09	$UVM2$	Swift+UVOT
ZTF18aavskep	2458277.8405	17.29	0.08	$1.984e-15$	$0.146e-15$	−19.21	0.08	$UVW1$	Swift+UVOT

Note—This table is available in its entirety in machine-readable format in the online journal. A portion is shown here for guidance regarding its form and content. Time is shown relative to the estimated epoch at which the extrapolated light curve (based on Equation A2 and Equation A1) is reaching zero, as derived in § 3.1 and shown in Table 1.

procedures using the FLOYDS data reduction pipeline[5] (Valenti et al. 2014).

Data from the Dual Imaging Spectrograph (DIS6) mounted on the 3.5 m Astrophysics Research Consortium (ARC) telescope at the Apache Point Observatory were reduced using standard procedures and calibrated to a standard star obtained the same night using the PyDIS package (Davenport 2018);

Data taken with the the Keck Low-Resolution Imaging Spectrometer (LRIS) (Oke et al. 1995). The data was reduced with the LRIS automated reduction pipeline[6].

3. ANALYSIS

3.1. *Epoch of zero flux*

In order to derive the epoch of zero flux of all the events, we used the `Photomanip`[7] package (released in the Appendix of this paper) to fit the r-band flux during the rise time (or the g-band fluxlight curve, when early r-band data points are not available) with an exponential function of the form

$$f = f_{\max}\{1 - \exp\left[(t_0 - t)/t_c\right]\} \ , \qquad (1)$$

and a power-law of the form

$$f = a(t - t_0)^n \ , \qquad (2)$$

(where t_0 is the extrapolated time of zero flux, $f_{\max}$ is the maximum flux, t_c is the characteristic rise time of the bolometric light curve). In each case, we chose the function giving the best fit, which allowed us to estimate the epochs at which the extrapolated light curves are reaching zero, which are used throughout this paper as the reference time t_0, and are summarized in Table 4. For each SN in our sample, the table shows the band in which the fit was performed (g or r, depending on how constraining the data are), the prior on t_0 is taken to be the time-interval between the most recent pre-explosion upper limit and the first detection. Table 4 also shows the 1σ confidence interval on t_0. The typical uncertainty on t_0 is of order 1 to a few days, with the exception of SN 2019cac (where no previous non-detection exists and for which we applied a broad conservative prior on t_0), for which it is higher than 20 days.

3.2. *Blackbody temperature, radius and bolometric luminosity*

Taking advantage of the multiple-band photometry coverage, we used the `PhotoFit`[8] tool (Soumagnac et al. 2019a) to derive the temperature and radius of the blackbody that best fits the photometric data at each epoch. The derived best-fit temperatures T_{BB} and radii r_{BB} are shown in Figure 3. We observe that seven objects of our sample exhibit a fast increase of the blackbody radius, a result in contrast with most previous observations. Indeed, many previously studied SNe IIn showed a constant blackbody radius (e.g., SN2010jl Ofek et al. 2014), consistent with the continuum photosphere being located in the unshocked optically thick CSM. In some cases a blackbody radius stalling after a short increase (e.g., 2005kj, 2006bo, 2008fq, 2006qq, Taddia et al. 2013; 2006tf, Smith et al. 2008) or even a shrinking blackbody radius (e.g., SN2005ip; SN2006jd, Taddia et al. 2013) were observed. Such observations were explained by the possible presence of clumps in the CSM

[5] https://github.com/svalenti/FLOYDS_pipeline

[6] http://www.astro.caltech.edu/dperley/programs/lpipe.html

[7] https://github.com/maayane/PhotoManip

[8] https://github.com/maayane/PhotoFit

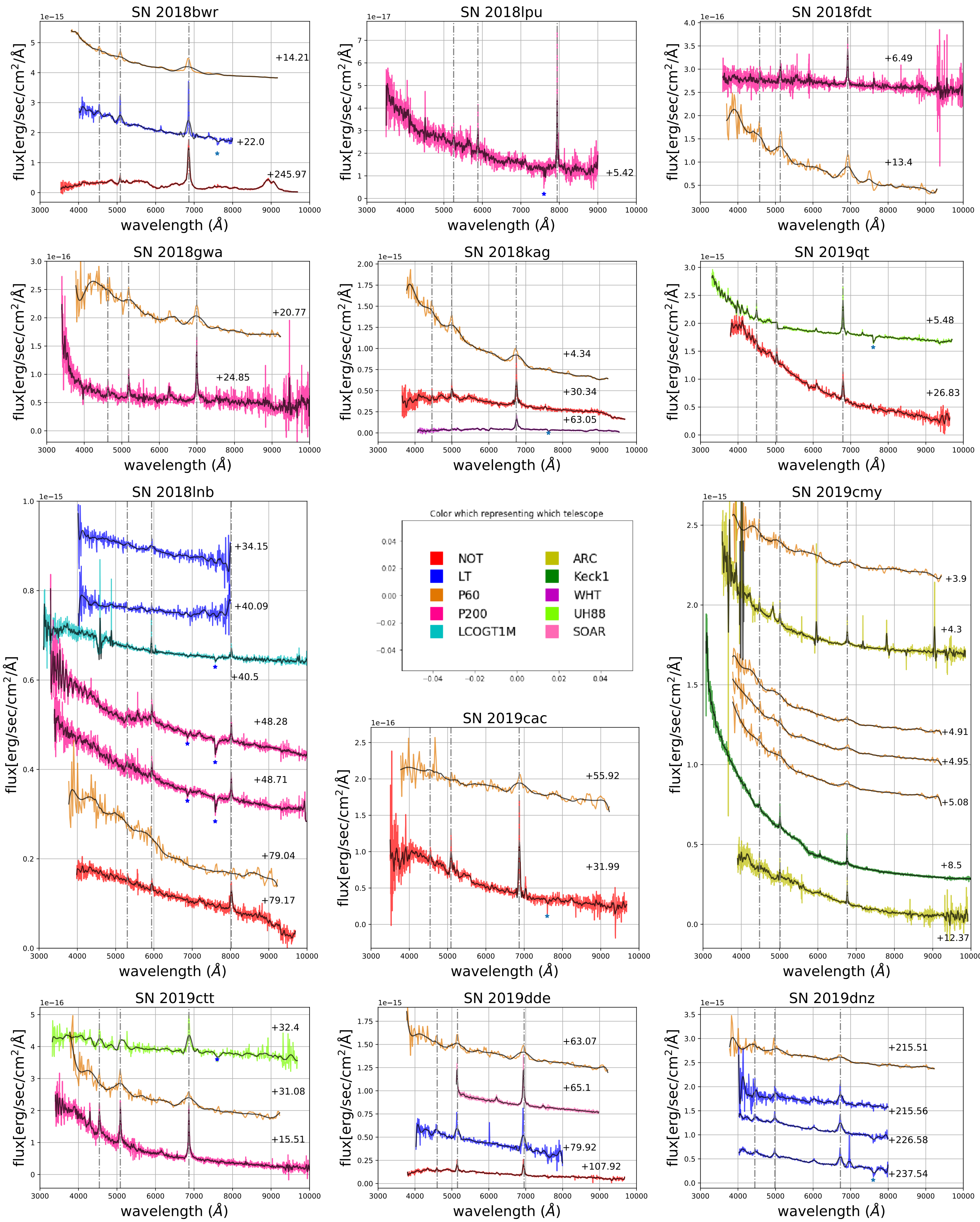

Figure 2. Optical spectra of all Type IIn SNe studied for this article. The dashed vertical lines show the Balmer series. The blue stars indicate telluric absorption.

Table 3. Summary of spectroscopic observations

Object	Date	Facility
SN 2018bwr	2018 Jun 02	P60 + SEDM
	2018 Jun 10	LT + SPRAT
	2019 Jan 19	NOT + ALFOSC
SN 2018lpu	2018 Jul 17	P200 + DBSP [1]
SN 2018fdt	2018 Aug 12	P60 + SEDM
	2018 Aug 19	P200 + DBSP
SN 2018gwa	2018 Oct 06	P60 + SEDM
	2018 Oct 10	P200 + DBSP
SN 2018kag	2018 Dec 24	P60 + SEDM
	2019 Jan 19	NOT + ALFOSC
	2019 Feb 20	WHT + ACAM
SN 2019qt	2019 Jan 13	UH88 + SNIFS *
	2019 Feb 04	NOT + ALFOSC
SN 2018lnb	2019 Jan 29	LT + SPRAT
	2019 Feb 04	LCOGT 2m + FLOYDS
	2019 Feb 04	LT + SPRAT
	2019 Feb 12	P200 + DBSP
	2019 Feb 12	P200 + DBSP
	2019 Mar 15	NOT + ALFOSC
	2019 Mar 15	P60 + SEDM
SN 2019cac	2019 Mar 14	P60 + SEDM
	2019 Apr 07	NOT + ALFOSC
SN 2019cmy	2019 Mar 29	P60 + SEDM
	2019 Mar 30	ARC + DIS
	2019 Mar 30	P60 + SEDM
	2019 Mar 30	P60 + SEDM
	2019 Mar 31	P60 + SEDM
	2019 Apr 03	Keck1 + LRIS
	2019 Apr 07	ARC + DIS
SN 2019ctt	2019 Apr 06	UH88 + SNIFS *
	2019 Apr 22	P60+SEDM
	2019 Apr 24	P200+DBSP
SN 2019dde	2019 Apr 14	P60 + SEDM
	2019 Apr 16	SOAR + Goodman *
	2019 May 01	LT + SPRAT
SN 2019dnz	2019 Apr 19	P60 + SEDM
	2019 Apr 19	LT + SPRAT
	2019 Apr 30	LT + SPRAT
	2019 May 11	LT + SPRAT

Note—The spectra marked with a star were obtained from the TNS and kindly made available to us by Anna V Payne, Michael A. Tucker (SCAT) and Dr. Regis Cartier. [1] The 600/4000 grism and 316/7500 grating were used for the blue and red cameras, respectively, with the D55 dichroic.

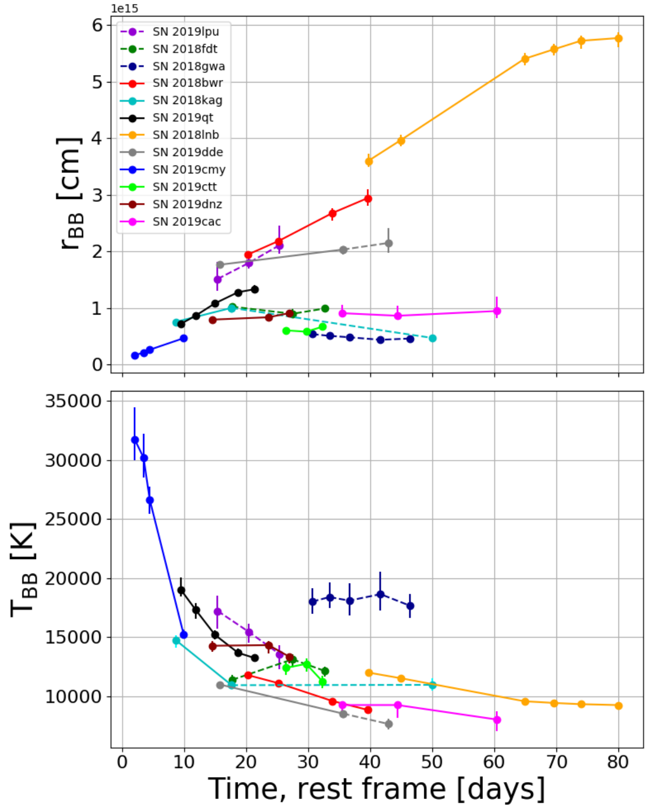

Figure 3. The evolution in time of: (1) the radius (upper panel), (2) the temperature (lower panel) of a blackbody with the same radiation as each of the twelve SNe in our sample. The points were obtained by fitting a blackbody spectrum to the observed photometry, after interpolating the various data sets to obtain data coverage of coinciding epochs. The errors were obtained with Monte Carlo Markov chain simulations. The dashed lines correspond to objects for which no late spectra was obtained in order to confirm that the CSM is optically thick. They should be taken cautiously.

that may expose underlying layers (Smith et al. 2008). PTF 12glz was not the only case were a fast increase of the blackbody radius was observed: three of the SNe IIn observed - in the UV - by de la Rosa et al. (2016) showed blackbody radii growing at comparable rates. This could be due to the fact that UV observations provide a better handle on the blackbody spectrum shape than visible light alone, suggesting that a fast increase of the blackbody radius of SNe IIn may be more common than suggested by visible-light surveys of these objects.

We further discuss and exploit the r_{BB} measurement in § 4.

Based on the measurement of r_{BB} and T_{BB}, we were able to derive the luminosity $L_{\rm BB} = 4\pi r_{\rm BB}^2 \sigma T_{\rm BB}^4$ of the blackbody fits, shown in Figure 4.

Table 4. Reference times fitting results

IAU Name	ZTF Name	model	band	most recent upper limit (JD)	t_0 (JD)	confidence interval (JD)
SN 2018lpu	ZTF18abgrlpv	power law	g	2458306.847	2458306.846	[2458306.845,2458307.330]
SN 2018fdt	ZTF18abltfho	exponent	r	2458334.665	2458336.338	[2458335.790,2458336.632]
SN 2018gwa	ZTF18abxbhov	exponent	g	2458374.969	2458376.524	[2458375.206, 2458376.526]
SN 2018bwr	ZTF18aavskep	exponent	r	2458257.521	2458257.527	[2458257.399, 2458257.644]
SN 2018kag	ZTF18acwzyor	power law	g	2458464.965	2458467.591	[2458466.373, 2458467.880]
SN 2019qt	ZTF19aadgimr	exponent	g	2458488.008	2458491.726	[2458491.634, 2458491.800]
SN 2018lnb	ZTF19aaadwfi	power law	g	2458467.972	2458475.834	[2458475.415, 2458478.945]
SN 2019cac	ZTF19aaksxgp	power law	g	2458521.778	2458521.937	[2458503.976,2458526.771]
SN 2019cmy	ZTF19aanpcep	exponent	g	2458567.983	2458568.505	[2458568.330,2458568.577]
SN 2019ctt	ZTF19aanfqug	exponent	r	2458541.796	2458550.011	[2458546.826,2458551.973]
SN 2019dde	ZTF19aaozsuh	power law	r	2458573.902	2458582.434	[2458580.024,2458582.710]
SN 2019dnz	ZTF19aaqasrq	exponent	r	2458581.995	2458583.441	[2458582.907,2458583.702]

NOTE—The "model" column specifies whether a power law (Equation A2) ore a concave exponent (Equation A1) gives the best fit. The "band" column specifies the band (g or r) used for the fit, and was chosen according to the amount of data available in each band. We then report the most recent non detection, which we use as the lower limit of our prior on t_0 (we use the most recent detection as the upper limit). For SN 2019cac, no previous non-detection exists, and so our prior interval is a time interval of 100 days before the first detection. The "t_0" column is the best fit time at which the flux reaches zero - the time used as an estimate of the explosion epoch. The confidence interval, shown in the last column, is defined here as the tightest intervals containing 68% of the probability and including our best-fit t_0 value.

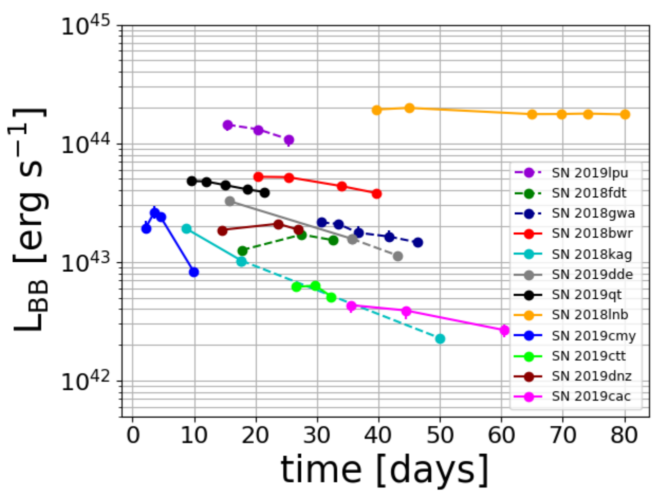

Figure 4. The evolution in time of the bolometric luminosity of a blackbody with the same radiation as each of the twelve SNe in our sample. The dashed lines correspond to objects for which no late spectra was obtained in order to confirm that the CSM is optically thick. They should be taken cautiously.

3.3. *Spectroscopy*

In this section, we only report the spectroscopic information that allow us to assess which photometric data are usable for our analysis of the CSM geometry. Indeed, the asphericity criterion proposed by Soumagnac et al. (2019b) is only applicable at times when the CSM surrounding the explosion is optically thick. To verify this, we require that the spectrum will be dominated by a blackbody continuum with no high velocity ($> 2000\,\mathrm{km\,s^{-1}}$) absorption and emission lines.

We can only include in our analysis multiple-band photometry that was collected before, or close to, the observation of a spectrum showing no evidence for high-velocity material. Unfortunately, we were unable to secure such spectroscopy for the SNe IIn ZTF18abgrlpv, ZTF18abltfho and ZTF18abxbhov, for which no spectra were taken after or close to the last *Swift* data point.

3.3.1. *SN 2018bwr*

The first two spectra show H_α, H_β and H_γ emission lines. In the last spectrum, we see prominent broad Ca II emission, blended with the O I $\lambda\,8446\,$Å feature. The numerous Fe lines are blended, exhibiting a pseudo-continuum around ∼5500 Å. Such a pseudo continuum is also seen e.g. in PTF 12glz (Soumagnac et al. 2019b) and in SN 2005 cl (Kiewe et al. 2012). We conclude from this that the spectra are dominated by interaction out to late times, and we can use all of the UV photometry for our analysis.

3.3.2. *SN 2018kag*

The first spectrum shows a blue continuum with Balmer emissions lines. The Balmer lines remain discernible at +30.3 d and the continuum becomes flat. At +63.10 d, higher velocity absorption and emission lines have appeared in the spectrum, hinting that the CSM may not be optically thick anymore. As a result, only the UV photometry taken between the first two spectra is usable for our analysis of the CSM geometry.

3.3.3. *SN 2019qt*

Distinct narrow H_α and H_β emission lines are visible in both spectra. H_γ emission is also visible, especially in the earlier spectrum. Since all the UV photometry was taken between the epochs of these two spectra, all of it is usable for our analysis.

3.3.4. *SN 2018lnb*

Narrow Balmer emission are visible in all spectra except for the first two spectra, in which the Ha component falls outside the spectral range of SPART/LT, and the SEDm/P60 spectrum which has low signal-to-noise. All of the UV photometric data is usable for our analysis.

3.3.5. *SN 2019cac*

In spite of the low resolution of the first spectrum, H_α emission is visible at +31.9 d. Strong emission lines of H_α, H_β and H_γ can be observed at +55.9 d. Although the last UV data point was taken after the second spectrum, we consider their epochs to be close enough so that all of the UV data can be used for our analysis.

3.3.6. *SN 2019cmy*

The narrow Balmer emission lines, that define the type IIn class, are the signature of an external physical phenomenon highly dependent on the surrounding environment, rather than of any intrinsic property of the explosion. In the case of "flash spectroscopy" events, these lines only persist for days, whereas in the case of SNe IIn they may still be visible in the spectrum for months or years. The type IIn class is not a well-defined category of objects, and in particular, the limit between flash-spectroscopy events and Type IIn SNe can be blurry, when the Balmer lines persist for weeks or a few months.

In the case of SN 2019cmy, prominent narrow Balmer emissions lines are visible at +4.9 d, with the characteristic broad wings of the Hα line, interpreted as the signature of electron scattering, clearly visible. Strong high-ionization emission lines of He II $\lambda\,4686\,\text{Å}$ only persists at +4.9 days. An excess on the blue side of the He II $\lambda\,4686\,\text{Å}$ coincides with the high-ionized C III $\lambda\,4650\,\text{Å}$. However, by +8.5 d, the C III $\lambda\,4650\,\text{Å}$ and He II $\lambda\,4686\,\text{Å}$ lines have completely disappeared, consistent with flash-ionized emissions. The Balmer lines decrease in strength with time: the H_γ $\lambda\,4341\,\text{Å}$ and H_δ $\lambda\,4102\,\text{Å}$ are marginally detected at +8.5 d and have disappeared by day +12.4. A spectrum taken two months after first light (and not shown in this paper) exhibits the features of a "normal" Type II SN, without any particular signature of CSM interaction.

Our geometrical analysis, which probes the shape of the CSM rather than its amount or the physical ways by which it was ejected, should still hold. All the UV photometry is usable for our analysis.

3.3.7. *SN 2019ctt*

Narrow Balmer lines (H_α, H_β, H_γ) are visible in all three spectra. The H_δ line is also visible in the higher resolution spectrum at +32.4 d. All the UV photometry is usable for our analysis.

3.3.8. *SN 2019dde*

The first spectrum, taken at +63.07 d with the SEDm/P60 shows narrow Balmer lines (H_α, H_β, H_γ, H_δ, H_ϵ). The three later spectra at +65.10 d, +79.92 d and +107.92 d show narrow H_α and H_β emission lines,

In the last spectrum, a narrow He $\lambda\,5876\,\text{Å}$ emission line is visible. Although the Balmer series is strongly dominated by narrow emission, the broad absorption at 5000-10000 $\mathrm{km\,s^{-1}}$ suggests that the ejecta have become visible, and the CSM is not completely optically thick anymore.

To account for this, we only use the first two UV epochs for our analysis.

3.3.9. *SN 2019dnz*

Narrow Balmer lines (H_α, H_β, H_γ) are visible in all three spectra. In addition, H_δ, H_ϵ emission lines can be seen in the last spectrum. All the UV photometry can be used for our analysis.

3.3.10. *Events with missing final spectra*

For three objects of our sample, we were unable to collect a spectrum showing no evidence for high-velocity material close to or after the last UV photometry epoch. For SN 2018 lpu, one spectrum was taken, where strong and narrow Balmer lines can be seen. Other interesting features include narrow emission of He II ($\lambda\,3203\,\text{Å}$, $\lambda\,4686\,\text{Å}$), [O II]$\lambda\,3727\,\text{Å}$, and [O III] $\lambda\,5007\,\text{Å}$. For both SN 2018fdt and SN 2018gwa, two spectra were obtained before any *Swift* photometry was taken. Both show prominent narrow Balmer emissions lines.

4. FRACTION OF SNE IIN SHOWING EVIDENCE FOR ASPHERICAL CSM

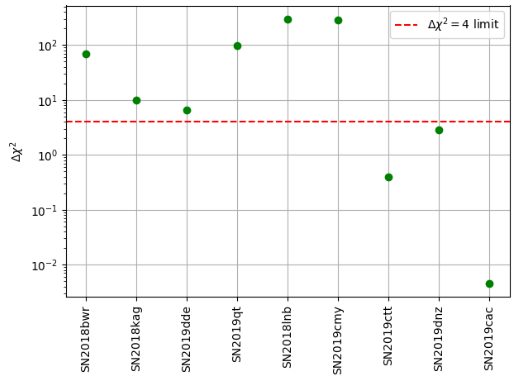

Figure 5. Result of the likelihood-ratio test (or chi-square difference test), when modeling the evolution of $r_{\rm BB}$ with a power law and with a flat function. The red dashed line shows the $\Delta\chi^2 = 4$ (i.e. 2σ) limit for one degree of freedom difference: objects with a $\Delta\chi^2$ limit above this line are better modeled by a non-zero power law (and hence show evidence for aspherical CSM), whereas objects below this line are better modeled by a flat line (i.e. show no evidence for aspherical CSM). Applying the criterion from Soumagnac et al. (2019b), six out of nine SNe IIn in our sample show evidence for aspherical CSM.

4.1. *Application of the asphericity criterion from Soumagnac et al. (2019b)*

Assessing whether the blackbody radius $r_{\rm BB}$, shown in Figure 3, is growing or not, is a model selection problem, i.e. we need to select between two models the one that best explains the data. Our first model is a power law function of the form $R = R_0\left(\frac{t}{t_0}\right)^n$, and our second model is a flat function of the form $R = R_0$ (i.e. $n = 0$). Since these models are nested, we can apply a likelihood-ratio test (or chi-square difference test) to discriminate between them. In Figure 5, we show the χ^2 difference between the two models derived for all objects. For six out of nine objects, $\Delta\chi^2 > 4$ i.e. the chi-square difference indicates that the increasing radius is more likely than the constant radius at a 2σ level. Therefore 66% of the SNe in our sample (taking into account only the SNe to which our analysis is applicable) show evidence for aspherical CSM.

4.2. *Correction for the non-uniform volume distribution of the SNe in our sample*

In Figure 6, we show the distribution of absolute magnitudes of the SNe IIn of our sample. The overall distribution (in blue) is comparable to previously published absolute luminosity distribution for SNe IIn (see e.g. Figure 17 in Richardson et al. 2014). However, the SNe showing no evidence for a rising $r_{\rm BB}$ are on the faint end of the distribution, i.e. located close to the observer. If we assume that in reality, both groups of SNe obey the same luminosity - and volume - distribution, the SNe showing no evidence for a rising $r_{\rm BB}$ appear to be under-represented in our sample, a fact that needs to be corrected for in the final probability calculation. A full relative rate calculation, taking into account a broader variety of selection effects, e.g. due to the cadence, the varying limiting magnitude of each image or the extinction at the location of the SN, is beyond the scope of this paper. Here, we simply estimate the relative probability p_i of finding the i^{th} SN IIn of our sample (SN$_i$) as

$$p_i = \frac{\frac{1}{V_{max,i}}}{\sum\limits_{j=1}^{9}\frac{1}{V_{max,j}}}\ , \qquad (3)$$

where $V_{max,i}$ is the maximum volume to which SN$_i$ can be observed, under the assumption of a constant limiting magnitude for the survey in the r, $m_{\rm lim} = 20.5$.

We find that although 66% of the SNe IIn to which our analysis is applicable exhibit a rising $r_{\rm BB}$, the corrected fraction of SNe IIn showing such feature is 35%. As this is a sufficient but not necessary condition for the surrounding CSM to be aspherical, 35% is a lower limit on the fraction of SNe IIn exploding in aspherical CSM.

5. CONCLUSIONS

We presented the first planned Ultra-Violet (UV) survey of the early evolution of type IIn supernovae (SNe IIn). Our sample consists of 12 SNe IIn discovered and observed with the Zwicky Transient Facility (ZTF) and followed-up in the UV by the Neil Gehrels Swift Observatory. All SNe were also spectroscopically followed-up: we present and release the spectroscopic data we collected.

The UV observations presented in this paper could help shed light on various aspects of the physical picture governing these events. For example, they may be used to better understand the explosion mechanism and the CSM properties (e.g., Ofek et al. 2013b), since the collisionless shock propagating in the CSM after the shock breakout (Ofek et al. 2010) is predicted to radiate most in the UV and X-rays.

Observations of SNe IIn at UV wavelengths provide a better handle on the bolometric luminosity, blackbody radius and blackbody temperature than visible-light observations alone. This may be a reason why the fast rising blackbody radius - which we observe for seven objects out of the twelve of our sample - was only observed in the past in works using UV observations of SNe IIn (de la Rosa et al. 2016; Soumagnac et al. 2019b). This result is in contrast with most previous observations

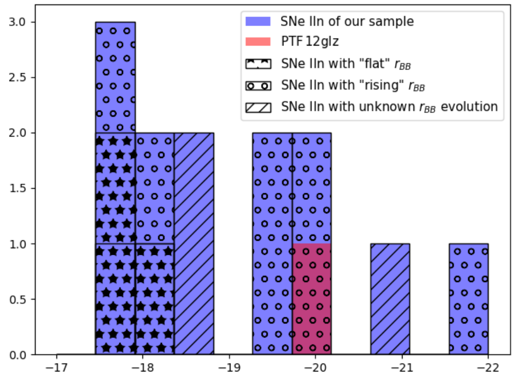

Figure 6. Absolute magnitude of the twelve SNe IIn of our sample and PTF 12glz. The blue histograms correspond to the entire sample and the red square corresponds to PTF 12glz. The star-patterned histograms correspond to the SNe IIn whose radius is better modeled by a flat function than by a power law (i.e. showing no evidence for aspherical CSM). These objects are at the faint end of the distribution, an effect we need to correct for in the calculation of their probability to occur (see § 4.2). The circle-patterned histograms correspond to the SNe IIn whose radius is better modeled by a power law (i.e. showing evidence for aspherical CSM). The line-patterned histograms correspond to the SNe IIn discussed in § 3.3.10, i.e. for which no late spectrum was collected and to which our analysis of the CSM geometry does not apply.

using visible-light observations alone, of either a constant, slowly rising (and then stalling) or even a shrinking blackbody radius.

We used the UV observations to address the following question: "what fraction of SNe IIn explode in aspherical CSM?". Indeed, although observations of SNe IIn are usually analyzed within the framework of spherically symmetric models of CSM, resolved images of stars undergoing considerable mass loss as well as well as polarimetry observations, suggest that asphericity is common, and should be taken into account for realistic modeling of these events. Constraining the geometrical distribution of the CSM surrounding the explosion is key to understanding the mass-loss processes occurring before the explosion and the nature of the yet-to-be determined progenitors of SNe IIn. Indeed, the presence of aspherical CSM around the progenitor is hard to explain by a simple wind, and requires to invoke other scenarios, such as episodic emission, rapid stellar rotation, or binarity.

We applied the criterion for asphericity introduced by Soumagnac et al. (2019b), stating that a fast increase of the blackbody effective radius, if observed at times when the CSM surrounding the explosion is still optically thick, may be interpreted as an indication that the CSM is aspherical. We find that two thirds of the SNe in our sample show evidence for aspherical CSM. After correcting for selection effects which leads SNe IIn not showing such evidence to be under-represented in our sample, we derive a conservative lower limit of 35% on the fraction of SNe IIn showing evidence for aspherical CSM.

As future wide-field transient surveys and the *ULTRASAT* UV satellite mission (Sagiv et al. 2014) are deployed, more UV observations of interracting SNe will be collected, allowing to build upon this survey and to refine the lower limit derived in this paper.

ACKNOWLEDGMENTS

M.T.S. thanks Charlotte Ward for useful discussions.

This work is based on observations obtained with the Samuel Oschin Telescope 48-inch and the 60-inch Telescope at the Palomar Observatory as part of the Zwicky Transient Facility project. ZTF is supported by the National Science Foundation under Grant No. AST-1440341 and a collaboration including Caltech, IPAC, the Weizmann Institute for Science, the Oskar Klein Center at Stockholm University, the University of Maryland, the University of Washington, Deutsches Elektronen-Synchrotron and Humboldt University, Los Alamos National Laboratories, the TANGO Consortium of Taiwan, the University of Wisconsin at Milwaukee, and Lawrence Berkeley National Laboratories. Operations are conducted by COO, IPAC, and UW.

We acknowledge the use of public data from the Swift data archive.

SED Machine is based upon work supported by the National Science Foundation under Grant No. 1106171

This paper shows observations made with the Nordic Optical Telescope, operated by the Nordic Optical Telescope Scientific Association at the Observatorio del Roque de los Muchachos, La Palma, Spain, of the Instituto de Astrofisica de Canarias.

Some of the data we present were obtained with ALFOSC, which is provided by the Instituto de Astrofisica de Andalucia (IAA) under a joint agreement with the University of Copenhagen and NOTSA. The Liverpool Telescope, located on the island of La Palma in the Spanish Observatorio del Roque de los Muchachos of the Instituto de Astrofisica de Canarias, is operated by Liverpool John Moores University with financial support from the UK Science and Technology Facilities Council.The ACAM spectroscopy was obtained as part of OPT/2018B/011.

A.G.-Y. is supported by the EU via ERC grant No. 725161, the Quantum Universe I-Core program, the ISF, the BSF Transformative program, IMOS via ISA and by a Kimmel award.

M.T.S. acknowledges support by a grant from IMOS/ISA, the Benoziyo center for Astrophysics at the Weizmann Institute of Science. This work was in part supported by the Scientific Discovery through Advanced Computing (SciDAC) program funded by U.S. Department of Energy Office of Advanced Scientific Computing Research and the Office of High Energy Physics. This research used resources of the National Energy Research Scientific Computing Center (NERSC), a U.S. Department of Energy Office of Science User Facility operated under Contract No. DE-AC02-05CH11231.

E.O.O is grateful for the support by grants from the Israel Science Foundation, Minerva, Israeli Ministry of Science, the US-Israel Binational Science Foundation, the Weizmann Institute and the I-CORE Program of the Planning and Budgeting Committee and the Israel Science Foundation.

C. F gratefully acknowledges support of his research by the Heising-Simons Foundation (#2018-0907).

APPENDIX

A. RELEASE OF THE `PHOTOMANIP` CODE

The `PhotoManip` tool, used to calculate the reference time for all the light curves and figures in this paper, is made available at `https://github.com/maayane/PhotoManip`.

The reference time is calculated as the epochs at which the extrapolated light curve is reaching zero. `PhotoManip` fits either the r-band or the g-band flux during the rise time with an exponential function of the form

$$f = f_{\rm max}\{1 - \exp\left[(t_0 - t)/t_c\right]\} \ , \tag{A1}$$

and a power-law of the form

$$f = a(t - t_0)^n \ , \tag{A2}$$

(where t_0 is the time of zero flux, $f_{\rm max}$ is the maximum flux, t_c is the characteristic rise time of the bolometric light curve). The fit uses the MCMC algorithm `emcee`(Foreman-Mackey et al. 2013).

REFERENCES

Aretxaga, I., Benetti, S., Terlevich, R. J., et al. 1999, MNRAS, 309, 343

Barnsley, R. M., Smith, R. J., & Steele, I. A. 2012, Astronomische Nachrichten, 333, 101

Bellm, E. C., Kulkarni, S. R., Graham, M. J., et al. 2019, Publications of the Astronomical Society of the Pacific, 131, 018002

Ben-Ami, S., Konidaris, N., Quimby, R., et al. 2012, in Society of Photo-Optical Instrumentation Engineers (SPIE) Conference Series, Vol. 8446, Ground-based and Airborne Instrumentation for Astronomy IV, 844686

Bilinski, C., Smith, N., Williams, G. G., et al. 2017, arXiv:1712.03370

Blagorodnova, N., Neill, J. D., Walters, R., et al. 2018, PASP, 130, 035003

Cardelli, J. A., Clayton, G. C., & Mathis, J. S. 1989, ApJ, 345, 245

Cartier, R., Briceno, C., Gomez, D., Espinoza, J., & Estay, O. 2019, The Astronomer's Telegram, 12671

Cenko, S. B., Fox, D. B., Moon, D.-S., et al. 2006, PASP, 118, 1396

Chevalier, R. A., & Irwin, C. M. 2012, ApJL, 747, L17

Chugai, N. N., & Danziger, I. J. 1994, MNRAS, 268, 173

Danziger, I. J., & Kjaer, K., eds. 1991, European Southern Observatory Conference and Workshop Proceedings, Vol. 37, Supernova 1987A and other supernovae

Davenport, J., d. M. W. T. D. 2018, PyDIS, https://github.com/TheAstroFactory/pydis, doi:10.5281/zenodo.58753

Davidson, K., & Humphreys, R. M. 1997, ARA&A, 35, 1

Davidson, K., & Humphreys, R. M., eds. 2012, Astrophysics and Space Science Library, Vol. 384, Eta Carinae and the Supernova Impostors

de la Rosa, J., Roming, P., Pritchard, T., & Fryer, C. 2016, ApJ, 820, 74

Fabian, A. C., & Terlevich, R. 1996, MNRAS, 280, L5

Fassia, A., Meikle, W. P. S., Vacca, W. D., et al. 2000, MNRAS, 318, 1093

Fassia, A., Meikle, W. P. S., Chugai, N., et al. 2001, MNRAS, 325, 907

Filippenko, A. V. 1997, ARA&A, 35, 309

Foreman-Mackey, D., Hogg, D. W., Lang, D., & Goodman, J. 2013, Publications of the ASP, 125, 306

Fremling, C. 2018, Transient Name Server Discovery Report, 2018-1463, 1

—. 2019a, Transient Name Server Discovery Report, 2019-414, 1

—. 2019b, Transient Name Server Discovery Report, 2019-586, 1

Fremling, C., Dugas, A., & Sharma, Y. 2018a, Transient Name Server Classification Report, 2018-1221, 1

—. 2018b, Transient Name Server Classification Report, 2018-1870, 1

—. 2019a, Transient Name Server Classification Report, 2019-329, 1

—. 2019b, Transient Name Server Classification Report, 2019-490, 1

—. 2019c, Transient Name Server Classification Report, 2019-581, 1

Fremling, C., & Sharma, Y. 2018, Transient Name Server Classification Report, 2018-762, 1

Fremling, C., Sollerman, J., Taddia, F., et al. 2016, A&A, 593, A68

Gal-Yam, A. 2017, Observational and Physical Classification of Supernovae, 195

Gal-Yam, A., & Leonard, D. C. 2009, Nature, 458, 865

Gal-Yam, A., Leonard, D. C., Fox, D. B., et al. 2007, ApJ, 656, 372

Gal-Yam, A., Arcavi, I., Ofek, E. O., et al. 2014, Nature, 509, 471

Gall, C., Hjorth, J., Watson, D., et al. 2014, Nature, 511, 326

Gehrels, N., Chincarini, G., Giommi, P., et al. 2004, ApJ, 611, 1005

Graham, M. J., Kulkarni, S. R., Bellm, E. C., et al. 2019, arXiv e-prints, arXiv:1902.01945

Hamuy, M., Folatelli, G., Morrell, N. I., et al. 2006, Publications of the Astronomical Society of the Pacific, 118, 2

Hoffman, J. L., Leonard, D. C., Chornock, R., et al. 2008, ApJ, 688, 1186

Katz, B., Sapir, N., & Waxman, E. 2011, arXiv:1106.1898

Khazov, D., Yaron, O., Gal-Yam, A., et al. 2016, ApJ, 818, 3

Kiewe, M., Gal-Yam, A., Arcavi, I., et al. 2012, ApJ, 744, 10

Leonard, D. C., Filippenko, A. V., Barth, A. J., & Matheson, T. 2000, ApJ, 536, 239

Levesque, E. M., Stringfellow, G. S., Ginsburg, A. G., Bally, J., & Keeney, B. A. 2014, AJ, 147, 23

Li, W.-D., Li, C., Filippenko, A. V., & Moran, E. C. 1998, IAUC, 6829

Masci, F. J., Laher, R. R., Rusholme, B., et al. 2019, PASP, 131, 018003

Mauerhan, J., Williams, G. G., Smith, N., et al. 2014, MNRAS, 442, 1166

Murase, K., Thompson, T. A., Lacki, B. C., & Beacom, J. F. 2011, PhRvD, 84, 043003

Murase, K., Thompson, T. A., & Ofek, E. O. 2014, MNRAS, 440, 2528

Nordin, J., Brinnel, V., Giomi, M., et al. 2019a, Transient Name Server Discovery Report, 2019-74, 1

—. 2019b, Transient Name Server Discovery Report, 2019-464, 1

—. 2019c, Transient Name Server Discovery Report, 2019-502, 1

Nyholm, A., Sollerman, J., Tartaglia, L., et al. 2019, arXiv e-prints, arXiv:1906.05812

Ofek, E. O., Rabinak, I., Neill, J. D., et al. 2010, ApJ, 724, 1396

Ofek, E. O., Sullivan, M., Cenko, S. B., et al. 2013a, Nature, 494, 65

Ofek, E. O., Fox, D., Cenko, S. B., et al. 2013b, ApJ, 763, 42

Ofek, E. O., Zoglauer, A., Boggs, S. E., et al. 2014, ApJ, 781, 42

Oke, J. B., Cohen, J. G., Carr, M., et al. 1995, PASP, 107, 375

Patat, F., Taubenberger, S., Benetti, S., Pastorello, A., & Harutyunyan, A. 2011, A&A, 527, L6

Payne, A. V., Tucker, M. A., Do, A., Shappee, B. J., & Huber, M. E. 2019, Transient Name Server Classification Report, 2019-97, 1

Prentice, S. J., Maguire, K., Magee, M. R., Clark, P., & Skillen, K. 2018, Transient Name Server Classification Report, 2018-1952, 1

Prentice, S. J., Maguire, K., Skillen, K., Magee, M. R., & Clark, P. 2019, Transient Name Server Classification Report, 2019-602, 1

Rahmer, G., Smith, R., Velur, V., et al. 2008, in Proc. SPIE, Vol. 7014, Ground-based and Airborne Instrumentation for Astronomy II, 70144Y

Reilly, E., Maund, J. R., Baade, D., et al. 2017, MNRAS, 470, 1491

Richardson, D., Jenkins, Robert L., I., Wright, J., & Maddox, L. 2014, AJ, 147, 118

Rigault, M., Neill, J. D., Blagorodnova, N., et al. 2019, A&A, 627, A115

Sagiv, I., Gal-Yam, A., Ofek, E. O., et al. 2014, AJ, 147, 79

Schlafly, E. F., & Finkbeiner, D. P. 2011, ApJ, 737, 103

Schlegel, E. M. 1990, MNRAS, 244, 269

Schlegel, E. M., & Petre, R. 2006, ApJ, 646, 378

Smith, N. 2014, ARA&A, 52, 487

Smith, N., Chornock, R., Li, W., et al. 2008, ApJ, 686, 467

Smith, N., Mauerhan, J. C., & Prieto, J. L. 2014, MNRAS, 438, 1191

Smith, N., Kilpatrick, C. D., Mauerhan, J. C., et al. 2017, MNRAS, 466, 3021

Soumagnac, M. T., Ganot, N., Gal-yam, A., et al. 2019a, arXiv e-prints, arXiv:1907.11252

Soumagnac, M. T., Ofek, E. O., Gal-yam, A., et al. 2019b, ApJ, 872, 141

Stathakis, R. A., & Sadler, E. M. 1991, MNRAS, 250, 786

Stoll, R., Prieto, J. L., Stanek, K. Z., et al. 2011, ApJ, 730, 34

Taddia, F., Stritzinger, M. D., Sollerman, J., et al. 2013, A&A, 555, A10

Tonry, J., Stalder, B., Denneau, L., et al. 2018a, Transient Name Server Discovery Report, 2018-695, 1

—. 2018b, Transient Name Server Discovery Report, 2018-1186, 1

Tucker, M. A., Payne, A. V., Do, A., Huber, M. E., & Shappee, B. J. 2019, Transient Name Server Classification Report, 2019-514, 1

Turatto, M., Cappellaro, E., Danziger, I. J., et al. 1993, MNRAS, 262, 128

Valenti, S., Sand, D., Pastorello, A., et al. 2014, MNRAS, 438, L101

van Dyk, S. D., Weiler, K. W., Sramek, R. A., & Panagia, N. 1993, ApJL, 419, L69

Wang, L., & Wheeler, J. C. 2008, ARA&A, 46, 433

Williams, C. L., Panagia, N., Van Dyk, S. D., et al. 2002, ApJ, 581, 396

Yaron, O., Perley, D. A., Gal-Yam, A., et al. 2017, Nature Physics, 13, 510

Zackay, B., Ofek, E. O., & Gal-Yam, A. 2016, ApJ, 830, 27